Journal of Materials Research and Technology 36 (2025) 9692–9698

Contents lists available at ScienceDirect

Journal of Materials Research and Technology

journal homepage: www.elsevier.com/locate/jmrt

Surface hardening of ductile austenitic lightweight steel through powder bed fusion 3D printing

Joonoh Moon [a,*], Hyun-Uk Hong [a], Hyungkwon Park [b], Hyo-Haeng Jo [b], Seong-Jun Park [b], Chansun Shin [c], Heung Nam Han [d], Myoung-Gyu Lee [d], Jae Suk Jeong [e], Bong Ho Lee [f], Chang-Hoon Lee [b]

[a] Department of Materials Science and Engineering, Changwon National University, 20 Changwondaehakro, Changwon, Gyeongnam, 51140, Republic of Korea
[b] Extreme Materials Research Institute, Korea Institute of Materials Science, 797 Changwondae-ro, Seongsan-gu, Changwon, Gyeongnam, 51508, Republic of Korea
[c] Department of Materials Science and Engineering, Myongji University, Yongin, 17058, Republic of Korea
[d] Department of Materials Science and Engineering & Research Institute of Advanced Materials, Seoul National University, Seoul, 08826, Republic of Korea
[e] Materials Technology Development Team, Doosan Enerbility, 22 Doosanvolvo-ro, Seongsan-gu, Changwon, Gyeongnam, 51711, Republic of Korea
[f] Advanced Analysis Team, Inst. of Next-Generation Semicond. Convergence Technol., Daegu Gyeongbuk Institute of Science and Technology, 333, Technojungang-daero, Hyeonpung-eup, Dalseong-gun, Daegu, 42988, Republic of Korea

ARTICLE INFO

Keywords:
Austenitic lightweight steel
3D printing
Powder bed fusion
κ-carbide
Surface hardening

ABSTRACT

To save energy and reduce CO_2 emissions, the lightweight design of structural components has recently become a global issue. Fe–Mn–Al–C based alloys with a low mass density have received considerable attention as structural materials enabling such lightweight designs. However, typical strength-ductility trade-off dilemma appears in Fe–Mn–Al–C lightweight steels. Dispersion of nano-sized Fe_3AlC-type κ-carbides achieves excellent tensile properties of high strength (~1 GPa) and large elongation (~50 %). However, further increase in strength (~1.2 GPa) caused by κ-carbide coarsening reduces elongation significantly (<10 %), limiting the potential applications of lightweight steels in structural parts that require ultrahigh strength and high ductility, such as wear-resistant components. Here, we resolve this drawback of lightweight steels by reinforcing the surface layer through 3D printing. The composition of base steel plate is Fe–30Mn–8Al-0.7C (wt%), and a lightweight steel powder with a relatively higher Al and C contents (Fe–30Mn-9.5Al-1.0C (wt%)) was then deposited on the surface of base steel plate through laser powder bed fusion (L-PBF). After L-PBF, an aging treatment led to more precipitation of κ-carbides in the surface layer, producing a functionally graded hard surface layer. A developed surface-hardened ductile lightweight steel thus has the potential to replace conventional wear-resistant steels, as it has excellent tensile ductility (51 %), high surface hardness (410 HV), high wear resistance, and 12 % lower mass density.

1. Introduction

Wear is the damage or removal of metal surfaces caused by destructive phenomena such as friction or erosion during the operation of mechanical devices. Decline in the functionality of devices due to wear causes severe economic losses, estimated at 1–4 % of the gross national product of an industrialized nation by abrasive wear [1]. Since Hadfield manganese steel with high hardness was first introduced in the late 19th century [2], various wear-resistant steels have been developed to overcome this problem [3–10]. To achieve outstanding wear-resistant characteristics, conventional wear-resistant steels generally consist of fully austenite or tempered martensite microstructure, which exhibit an excellent balance of strength and ductility. Despite their popularity and success, more advanced characteristics are now being demanded of wear-resistant steels, *i.e.*, lower mass density and higher ductility without loss of hardness.

In particular, the lightweighting design of structural components is essential for improving the efficiency of energy-conversion devices [11]. In addition, an increase in hardness to obtain wear-resistance characteristics in conventional steels decreases ductility significantly, the so-called 'strength-ductility trade-off dilemma'. Herein, we solve these two challenges ahead of conventional wear-resistant steels by

* Corresponding author.
E-mail address: mjo99@changwon.ac.kr (J. Moon).

https://doi.org/10.1016/j.jmrt.2025.05.174
Received 15 March 2025; Received in revised form 17 May 2025; Accepted 19 May 2025
Available online 20 May 2025

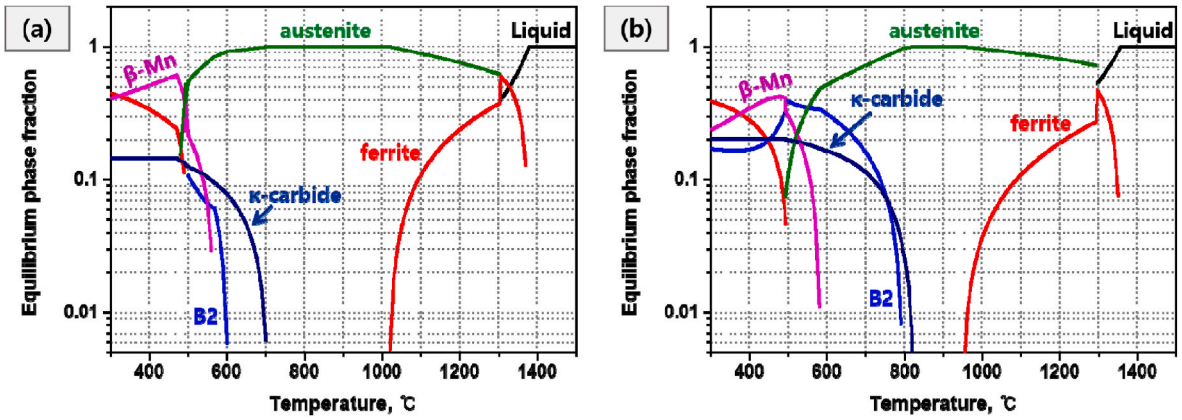

Fig. 1. Equilibrium phase diagram: (a) the LWS plate with the composition of Fe–30Mn–8Al-0.7C (wt.%) and (b) the LWS powder with the composition of Fe–30Mn-9.5Al-1.0C (wt.%).

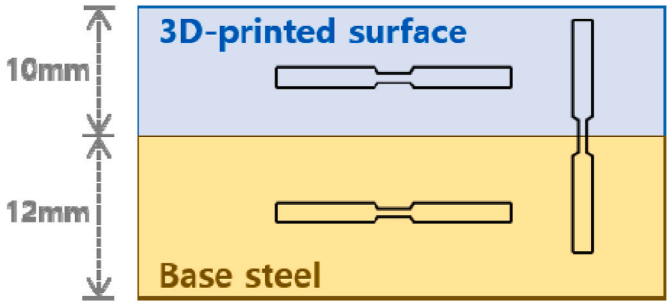

Fig. 2. Schematic diagram showing sampling location of the micro-tensile test specimens.

introducing austenitic Fe–Mn–Al–C lightweight steel and a 3D printing process. Austenitic Fe–Mn–Al–C steels exhibit an excellent balance between strength and ductility with a low mass density [11–14]. Al effectively reduces the density of steel and significantly increases the strength of Fe–Mn–Al–C steels owing to precipitation strengthening by the formation of nano-sized Fe_3AlC-type κ-carbides. However, the strength-ductility trade-off dilemma also appears in Fe–Mn–Al–C steels, *i.e.*, the precipitation of coarse intergranular κ-carbides by adding excessive Al results in a significant loss of ductility [11]. 3D printing is an additive manufacturing process that builds metal structures layer-by-layer [15–17]. Through 3D printing, a dissimilar surface layer that differs from the base steel can be formed.

Considering these facts, we designed a new type of lightweight steel with excellent tensile ductility and high surface hardness by creating a selectively hardened surface. We call this alloy surface-hardened ductile lightweight steel. To develop this alloy, we selected the base steel plate of a ductile austenitic lightweight alloy with the composition of Fe–30Mn–8Al-0.7C (wt%) and then deposited a lightweight steel powder with a relatively higher Al and C contents (Fe–30Mn-9.5Al-1.0C (wt %)) on the surface of the base steel plate through laser powder bed fusion (L-PBF). Finally, an aging treatment after L-PBF produced a functionally graded hard surface layer owing to the acceleration of κ-carbide precipitation in the surface layer.

2. Materials and methods

Ductile austenitic Fe–30Mn–8Al-0.7C lightweight steel (LWS) plate was prepared as the base steel. It was fabricated using commercial vacuum induction melting (VIM) and hot-rolling processes. First, an ingot sample was prepared using a VIM furnace. After reheating for 2 h at 1050 °C, the ingot sample was hot-rolled into the base steel sample with a thickness of 12 mm.

Next, to deposit a hard layer on the surface of base steel plate, the L-PBF 3D printing process was used. A metal powder with the composition Fe–30Mn-9.5Al-1.0C (wt%) was prepared through gas atomization and then sieved to isolate powder suitable for L-PBF. The mean particle size of the separated powder was 24.2 μm. Details of the PBF process include a laser power of 170 W, a scan speed of 900 mm/s, a hatch distance of 80 μm, and a layer thickness of 30 μm. Finally, a thickness of 3D-printed surface layer was 5 mm.

After L-PBF, the samples were first solution-treated for 2 h at 1050 °C and then water-quenched. It should be noted that a solution treatment temperature of 1050 °C was selected within the austenite temperature region of the LWS plate considering the equilibrium phase diagram. Fig. 1(a) and (b) show the equilibrium phase diagrams of the LWS plate

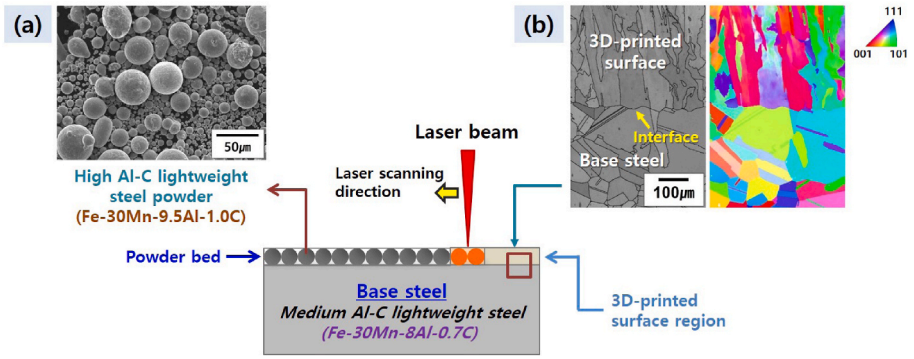

Fig. 3. Schematic illustration for manufacturing surface-hardened ductile lightweight steel via L-PBF: (a) SEM micrograph of Fe–30Mn-9.5Al-1.0C metal powder used for L-PBF and (b) band contrast image and IPF map obtained from EBSD analysis near the interface between base steel and surface layer deposited by L-PBF.

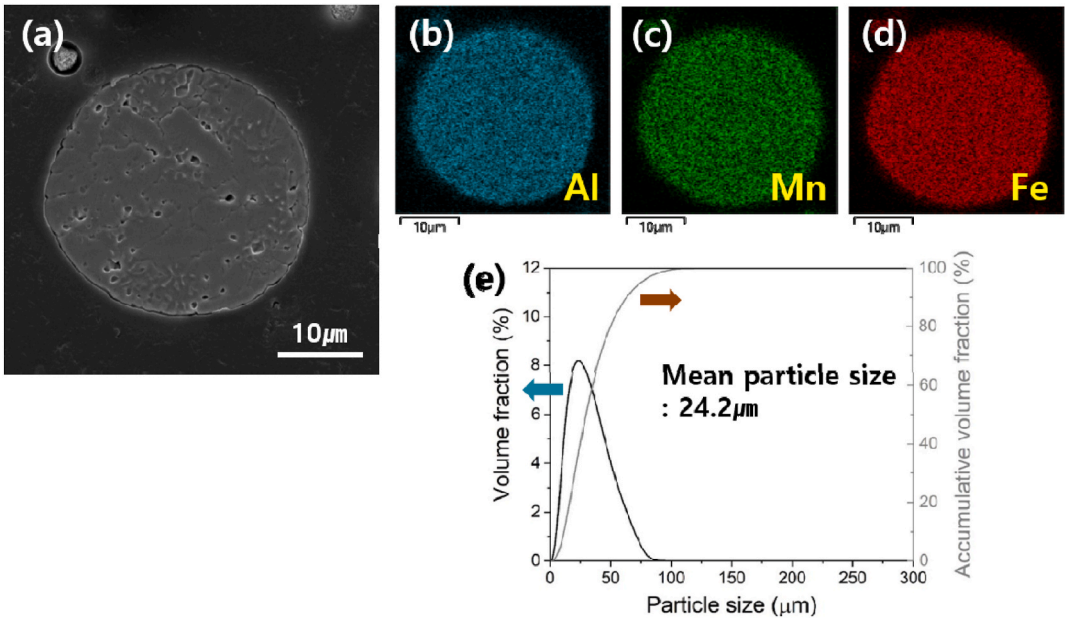

Fig. 4. Metal powder used for PBF: (a) SEM image, (b–d) EDS mapping for Al, Mn, and Fe in metal powder, and (e) size distribution of metal powder feedstock.

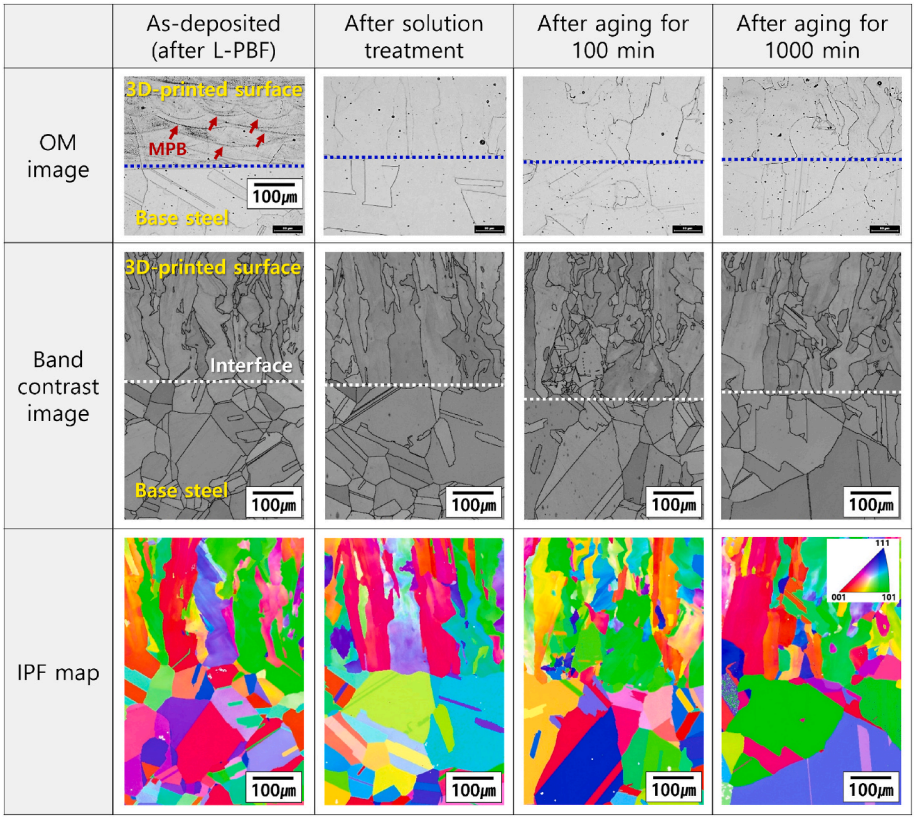

Fig. 5. Microstructure evolution of printed surface-hardened ductile lightweight steel during the solution and aging treatments.

and the LWS powder, respectively. As shown in Fig. 1(a), the LWS plate is expected to have a single austenite phase at 1050 °C. In the case of the LWS powder (Fig. 1(b)), the temperature range of austenite is narrow compared to the LWS plate, while the ferrite region is wider. This is because the LWS powder includes a higher amount of Al, which is a ferrite stabilizer. Next, to make a functionally graded material consisting of a hard surface on ductile base steel plate, the solution-treated samples were aged for various periods (30, 100, 1000 min) at 550 °C.

The microstructures of the samples after solution and aging treatments were investigated through optical microscopy (OM), scanning electron microscopy (SEM), transmission electron microscopy (TEM), and electron backscatter diffraction (EBSD) analyses. For the OM and SEM observations, the samples were first mechanically polished and then etched in a mixed solution of 100 ml ethanol and 4 ml nitric acid. For TEM observations, thin foil specimens were prepared by twin-jet electrolytic polishing at 20 V and 195 mA with a mixed solution of

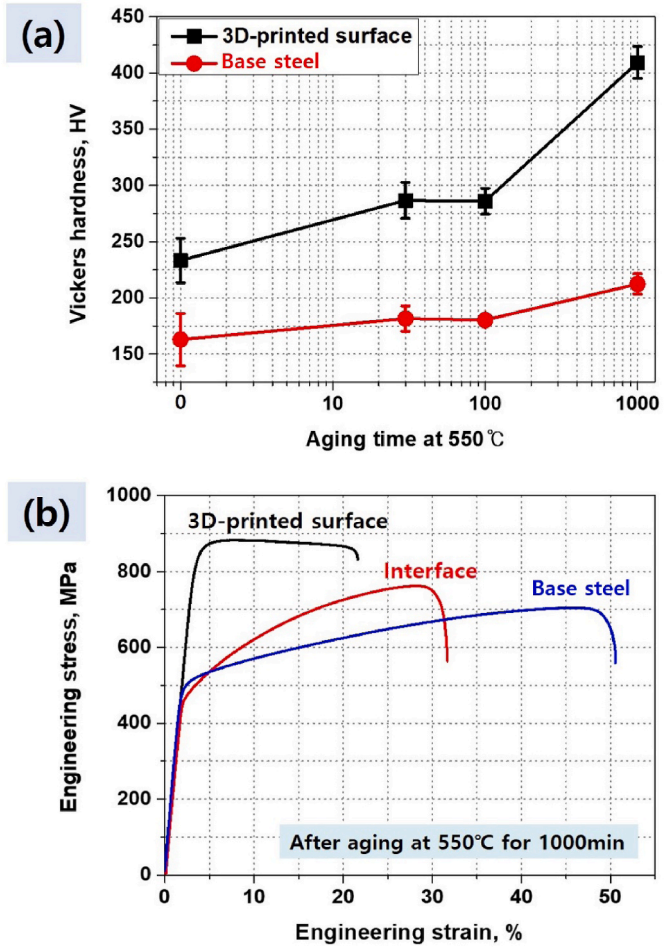

Fig. 6. Mechanical properties of surface-hardened ductile lightweight steel: (a) changes in hardness at the surface and in the base steel with increasing aging time at 550 °C and (b) tensile properties at each location of the sample aged for 1000 min at 550 °C.

10 % perchloric acid and 90 % methanol at −30 °C. The samples for EBSD analysis were prepared by mechanical polishing using a colloidal silica suspension. The distribution of the κ-carbide in the base steel and 3D-printed surface was analyzed using atom probe tomography (APT) with a CAMECA LEAP 4000X HR. Tip specimens for APT analysis were prepared using focused ion beam (FIB) equipment with an FEI Helios NanoLab G3 UC. The tip specimens were then held in a vacuum of 2.0×10^{-11} Torr at −223.15 °C (50 K), after which they were field-evaporated at a detection rate of 1.0 % with 355 nm UV laser at a laser pulse energy of 100 pJ and a laser pulse rate of 125 kHz. APT data were analyzed using the Interactive Visualization and Analysis Software (IVAS 3.8.4) of CAMECA instruments.

The stress-strain response of the samples was evaluated by tensile testing at a nominal strain rate of 6.5×10^{-3} s^{-1}. For tensile testing, micro-tensile specimens were machined. Fig. 2 shows sampling location of micro-tensile test specimens. As shown in Fig. 2, a 10 mm thick 3D-printed surface was additionally deposited on the base steel to perform micro-tensile tests as each location (base steel, 3D-printed surface, and their interface). The length of the gauge was 5.12 mm, the width of the reduced section was 1 mm, and the overall length of the specimen was 16 mm.

Finally, we performed wear resistance tests using a ball-on-disc apparatus. The test was conducted on the base steel and the 3D-printed surface with the reference material (commercial 400HV-grade wear-resistant steel) under the following conditions: Si_3N_4 ball as the counter material, applied load of 5 N, rotational speed of 100 RPM, wear radius of 5 mm, and a total of 50,000 revolutions. The wear resistance of the samples was evaluated by measuring the weight loss before and after testing.

3. Results and discussion

3.1. Base steel plate and metal powder used for L-PBF

Fig. 3 shows a schematic illustration of surface-hardened ductile lightweight steel manufactured through the L-PBF 3D printing process. For the base steel plate, we selected a Fe–30Mn–8Al-0.7C (wt%) lightweight steel with an austenite matrix because of its excellent ductility (65 % in solution-treated state) and high tensile strength (757 MPa in solution-treated state) at low mass density. To create a hard layer on the surface of the base steel plate, we performed PBF 3D printing using lightweight steel powder with the composition Fe–30Mn-9.5Al-1.0C (wt %), which contains higher Al and C contents than the base steel plate. Fig. 3(a) shows an SEM micrograph of the lightweight steel powder used in this investigation. Through the gas atomization process, spherical powders were fabricated and powders with a size range of 10–45 μm were then separated for the L-PBF process. Fig. 4 shows the distribution of alloying elements inside the powder and their size distribution. As shown in Fig. 4(b–d), all elements were distributed homogeneously in the powder, and the mean size of the powder was 24.2 μm (Fig. 4(e)). Fig. 3(b) shows a band contrast image and inverse pole figure (IPF) map obtained from EBSD analysis at the interface between the base steel plate and the 3D-printed surface layer.

3.2. Microstructure and strength change during the heat treatment

To develop a functionally graded austenitic lightweight steel with a ductile matrix and a hard surface at a low mass density, we carried out a solution and aging heat treatment after L-PBF. The aging treatment led to the precipitation of κ-carbides, and such behavior was accelerated at the 3D-printed surface region owing to higher Al and C content, facilitating selective hardening of the surface layer compared to the base steel. Several previous studies have reported the effects of Al and C on the precipitation behavior of κ-carbide in Fe–Mn–Al–C-based lightweight steels [11, 18–20]. Al and C constitute Fe_3AlC-type κ-carbide, and thus increasing the Al and C contents enhances the driving force for precipitation of κ-carbide.

Fig. 5 shows the changes of microstructures during the solution and aging treatments. As shown in Fig. 5, a sound 3D-printed surface layer was obtained and the interface between the base steel and the 3D-printed surface layer was well connected without defects. The melt pool boundaries (MPBs) were observed at the 3D-printed surface layer immediately after L-PBF and disappeared during the solution heat treatment. The base steel had coarse equiaxed grains, while the 3D-printed surface layer had a columnar grain that grew in a direction perpendicular to the MPBs (see the band contrast and IPF maps in Fig. 5). This growth direction of columnar grains vertical to the MPBs is same as heat conduction direction caused by the large temperature gradient. In addition, Fig. 5 shows that there was no noticeable change in texture during the solution and aging treatments, indicating that the recrystallization did not occur during heat treatments.

Fig. 6(a) shows the changes in Vickers hardness at the surface layer and in the base steel with an increase in aging time at 550 °C. It should be noted that the hardness values shown in Fig. 6(a) were measured at the 3D-printed surface layer and the base steel region on the cross-sectional area. As the aging progressed, the strength of both the base steel and the 3D-printed surface layer increased, and this aging hardening occurred more in the 3D-printed surface layer. As mentioned above, the different aging hardening behavior of the base steel and 3D-printed surface layer was attributable to a change in the precipitation kinetics of κ-carbide depending on Al and C content, *i.e.*, hardening in the 3D-printed surface layer occurred faster than that in the base steel

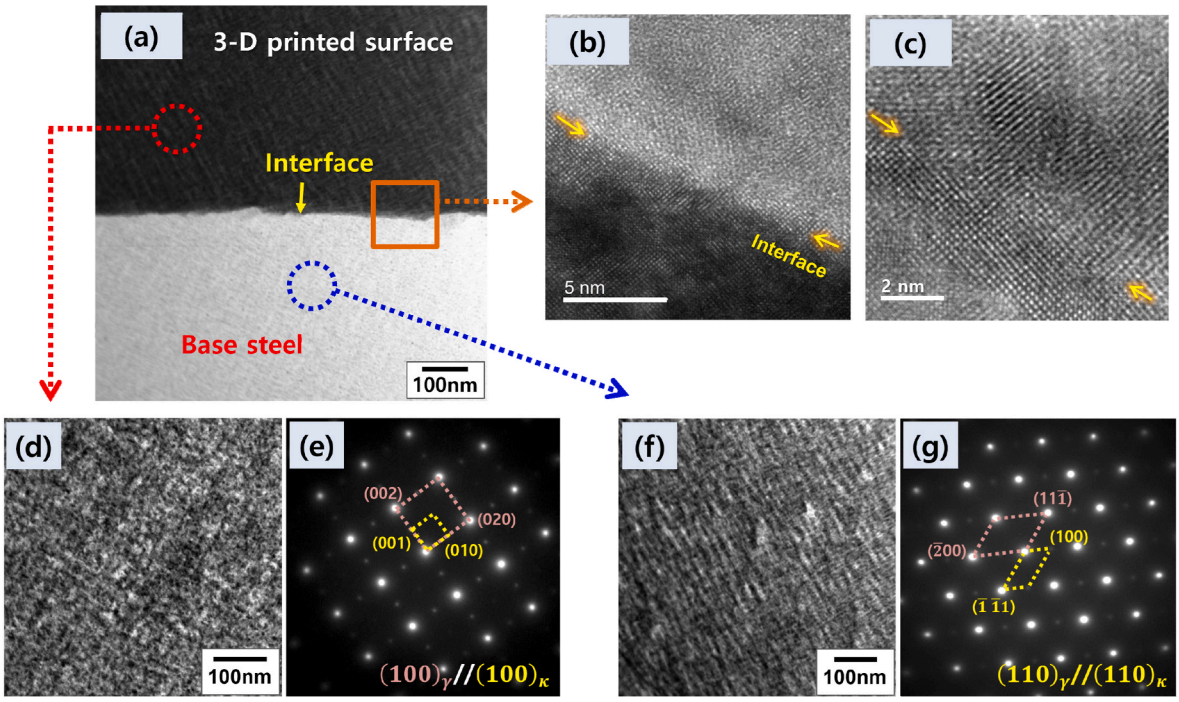

Fig. 7. TEM micrographs of surface-hardened ductile lightweight steel near the interface between the base steel plate and the 3D-printed surface layer after the aging for 1000 min at 550 °C. (a) STEM image, (b and c) high-resolution TEM image, (d and e) dark-field image and SAD pattern analysis in the 3D printed surface region, and (f and g) dark-field image and SAD pattern analysis in the base steel plate.

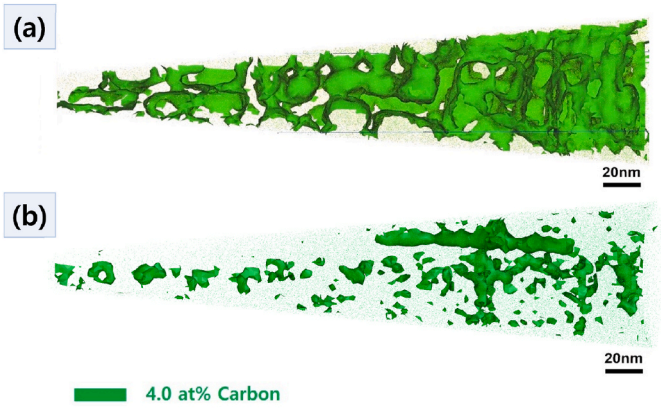

Fig. 8. Results of APT analyses. Iso-concentration surface images (a) at the 3D-printed surface region and (b) in the base steel after the aging for 1000 min at 550 °C.

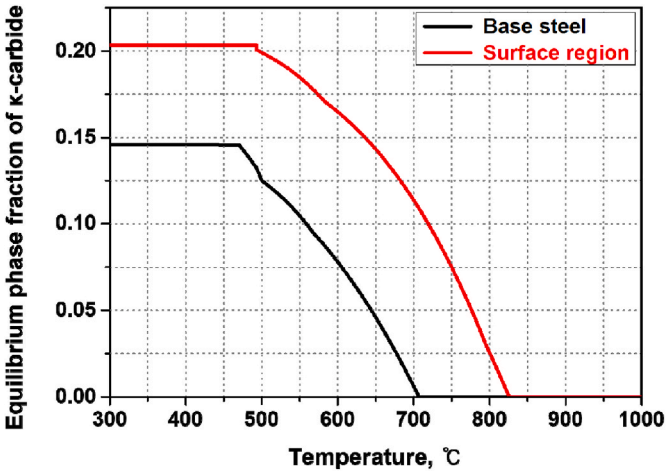

Fig. 9. Equilibrium phase fraction of κ-carbide in the base steel plate and at the 3D-printed surface layer.

due to the acceleration of κ-carbide precipitation in the 3D-printed surface layer by its higher Al and C content. Fig. 7(d and e) and 7(f–g) show TEM dark-field images and selected area diffraction (SAD) patterns in the 3D-printed surface layer and the base steel plate, respectively, after the aging for 1000 min at 550 °C. These results indicate that nanosized κ-carbides precipitated within the austenite matrix. To quantitatively compare the fraction of κ-carbide in the 3D-printed surface layer and the base steel plate, the atom probe tomography (APT) analyses was carried out. Fig. 8 shows iso-concentration surface images obtained from APT analyses of the sample aged for 1000 min at 550 °C. The κ-carbides can be distinguished from the matrix by the 4 at.% C iso-concentration surface. It should be noted that 4 at.% C is much lower that the C content in κ-carbide, but same approach with this study in APT analyses has been reported in many previous papers [11, 21–23]. These approaches have been accepted as reliable by comparison of the actual size of the κ-carbide with the APT observation results. As expected, there was more κ-carbide precipitated in the 3D-printed surface layer (Fig. 8(a)) than in the base steel (Fig. 8(b)). A thermodynamic calculation also predicts that the κ-carbide may precipitate more in the 3D-printed surface layer, as shown in Fig. 9. These results indicate that the 3D-printed surface layer achieved a considerably higher strength than the base steel after the aging due to the greater precipitation of κ-carbides, as shown in Fig. 6(a). As a result, we achieved a ductile lightweight steel with a high surface hardness of 400HV after the aging for 1000 min at 550 °C.

Fig. 6(b) shows the results of tensile tests at different locations of the sample aged for 1000 min at 550 °C. The base steel has an excellent balance between high yield strength (460 MPa) and high ductility (50.5 %). The 3D-printed surface layer exhibits an ultra-high yield strength

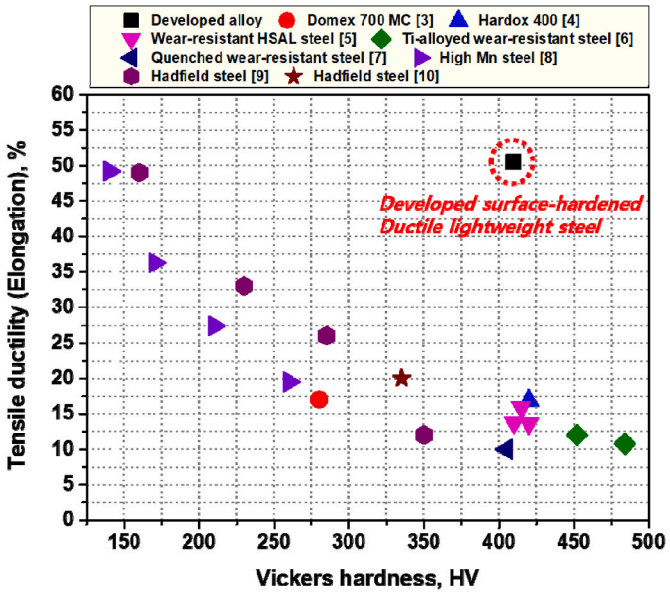

Fig. 10. Comparison of the Vickers hardness at the surface layer and tensile ductility of the surface-hardened ductile lightweight steel to those of conventional wear-resistant steels.

(770 MPa) and suitable tensile ductility (21.6 %). Despite the strengthening effect of κ-carbide precipitation, coarse intergranular precipitation did not occur in the 3D-printed surface layer (see Fig. 7 (a–c)), allowing for high tensile ductility. A previous study [24] reported a significant drop in tensile ductility due to the coarse intergranular precipitation of κ-carbides. Meanwhile, as shown in Fig. 6(b), the interface has tensile properties between those of the base steel and the 3D-printed surface layer, indicating that the 3D-printed surface layer is well bonded to the base steel with a dilution of alloying elements. Fig. 7 (b–c) show a high-resolution TEM image near the interface, indicating that a coherent interface is formed by epitaxial solidification during 3D printing [25,26], as shown in Fig. 5. That is, at the interface, the atoms of the base steel and the 3D-printed surface layer are perfectly matched and have same orientation, as shown in Fig. 7(c).

To confirm the potential of the developed alloy, we compared the surface hardness and tensile ductility of the developed alloy to those of conventional wear-resistant steels. Fig. 10 shows the tensile ductility versus surface hardness of the developed surface-hardened ductile lightweight steel compared to conventional wear-resistant steels. Apparently, conventional alloys typically exhibit a trade-off relationship between surface hardness (strength) and ductility. However, the new surface-hardened ductile lightweight steel has a significantly higher surface hardness while maintaining high ductility in the matrix than conventional wear-resistant steels.

Finally, we performed wear resistance tests on the base steel after aging for 1000 min and the 3D-printed surface after aging for 1000 min with commercial 400HV-grade wear-resistant steel under the applied load of 5 N, rotational speed of 100 RPM, wear radius of 5 mm, and a total of 50,000 revolutions. The weight loss before and after testing was measured as follows: 0.001 mg for commercial wear-resistant steel, 0.005 mg for the base steel, and 0.001 mg for the 3D-printed surface. These results indicate that the 3D-printed surface developed in this study exhibits significantly improved wear resistance compared to the base steel and a performance level comparable to the commercial wear-resistant steel. This confirms the potential of surface modification for enhancing the wear properties of lightweight steels.

With this functionally graded alloy design, surface-hardened ductile lightweight steel has the advantages of both wear-resistant steel and lightweight steel, with excellent tensile ductility (51 %), high surface hardness (410 HV), and a significant reduction in mass density (12 %) compared to general steels.

4. Conclusion

In summary, we designed a new class of alloy that is lightweight, highly ductile, and surface-hardened, to compete with conventional wear-resistant steels. The developed surface-hardened ductile lightweight steel is based on a ductile austenitic lightweight steel matrix of Fe–30Mn–8Al-0.7C (wt%). The surface layer was deposited through L-PBF 3D printing with a lightweight steel powder containing higher Al and C content (Fe–30Mn-9.5Al-1.0C (wt%)). After 3D printing, the aging treatment promoted greater precipitation of κ-carbide in the surface layer, achieving a functionally graded hard surface layer with a ductile matrix. This functionally graded lightweight steel thus has the potential to replace conventional wear-resistant steels owing to its superior tensile ductility (51 %) at high surface hardness (410 HV), high wear resistance and 12 % lower mass density.

Declaration of competing interest

The authors declare that they have no known competing financial interests or personal relationships that could have appeared to influence the work reported in this paper.

Acknowledgements

J. Moon was supported by the Basic Science Research Program through the National Research Foundation of Korea funded by the Ministry of Science & ICT (NRF-2022R1A2B5B02001852).

References

[1] Davis JR. Surface engineering for corrosion and wear resistance. Materials Park, OH, USA: ASM International; 2001.
[2] Weeks JD. Hadfield's manganese steel. Science 1888;12:284–6. https://doi.org/10.1126/science.ns-12.306.284.b.
[3] Denisa M, Michal J, Tibor V, Lýdia FD, František N. Examination of fatigue life of HSLA Domex 700 MC welded joints. Transp Res Procedia 2021;55:533–7. https://doi.org/10.1016/j.trpro.2021.07.018.
[4] Gupta A, Sharma V, Kumar P, Thakur A. Investigating the effect of ferritic filler materials on the mechanical and metallurgical properties of Hardox 400 steel welded joints. Mater Today Proc 2021;39:1640–6. https://doi.org/10.1016/j.matpr.2020.05.788.
[5] Mondal J, Das K, Das S. An investigation of mechanical property and sliding wear behaviour of 400Hv grade martensitic steels. Wear 2020;458–459:203436. https://doi.org/10.1016/j.wear.2020.203436.
[6] Kostryzhev AG, Killmore CR, Yu D, Pereloma EV. Martensitic wear resistant steels alloyed with titanium. Wear 2020;446–447:203203. https://doi.org/10.1016/j.wear.2020.203203.
[7] Ojala N, Valtonen K, Antikainen A, Kemppainen A, Minkkinen J, Oja O, Kuokkala VT. Wear performance of quenched wear resistant steels in abrasive slurry erosion. Wear 2016;354–355:21–31. https://doi.org/10.1016/j.wear.2016.02.019.
[8] Mousavi Anijdan SH, Sabzi M, Najafi H, Jafari M, Eivani AR, Park N, Jafarian HR. The influence of aluminum on microstructure, mechanical properties and wear performance of Fe–14%Mn–1.05%C manganese steel. J Mater Res Technol 2021;15:4768–80. https://doi.org/10.1016/j.jmrt.2021.10.054.
[9] Jafarian HR, Sabzi M, Mousavi Anijdan SH, Eivani AR, Park N. The influence of austenitization temperature on microstructural developments, mechanical properties, fracture mode and wear mechanism of Hadfield high manganese steel. J Mater Res Technol 2021;10:819–31. https://doi.org/10.1016/j.jmrt.2020.12.003.
[10] Wang W, Song R, Peng S, Pei Z. Multiphase steel with improved impact-abrasive wear resistance in comparison with conventional Hadfield steel. Mater Des 2016;105:96–105. https://doi.org/10.1016/j.matdes.2016.05.056.
[11] Moon J, Ha HY, Kim KW, Park SJ, Lee TH, Kim SD, Jang JH, Jo HH, Hong HU, Lee BH, Lee YJ, Lee C, Suh DW, Han HN, Raabe D. A new class of lightweight, stainless steels with ultra-high strength and large ductility. Sci Rep 2020;10:12140. https://doi.org/10.1038/s41598-020-69177-7.
[12] Kim SH, Kim H, Kim NJ. Brittle intermetallic compound makes ultrastrong low-density steel with large ductility. Nature 2015;518:77–9. https://doi.org/10.1038/nature14144.
[13] Kim H, Suh DW, Kim NJ. Fe–Al–Mn–C lightweight structural alloys: a review on the microstructures and mechanical properties. Sci Technol Adv Mater 2013;14:1–11. https://doi.org/10.1088/1468-6996/14/1/014205.

[14] Yao MJ, Welsch E, Ponge D, Haghighat SMH, Sandlöbes S, Choi P, Herbig M, Bleskov I, Hickel T, Lipinska-Chwalek M, Shanthraj P, Scheu C, Zaefferer S, Gault B, Raabe D. Strengthening and strain hardening mechanisms in a precipitation-hardened high-Mn lightweight steel. Acta Mater 2017;140:258–73. https://doi.org/10.1016/j.actamat.2017.08.049.

[15] Martin JH, Yahata BD, Hundley JM, Mayer JA, Schaedler TA, Pollock TM. 3D printing of high-strength aluminium alloys. Nature 2017;549:365–9. https://doi.org/10.1038/nature23894.

[16] Murray SP, Pusch KM, Polonsky AT, Torbet CJ, Seward GGE, Zhou N, Forsik SAJ, Nandwana P, Kirka MM, Dehoff RR, Slye WE, Pollock TM. A defect-resistant Co–Ni superalloy for 3D printing. Nat Commun 2020;11:4975. https://doi.org/10.1038/s41467-020-18775-0.

[17] Zhang D, Qiu D, Gibson MA, Zheng Y, Fraser HL, StJohn DH, Easton MA. Additive manufacturing of ultrafine-grained high-strength titanium alloys. Nature 2019;576:91–5. https://doi.org/10.1038/s41586-019-1783-1.

[18] Chen S, Rana R, Haldar A, Ray RK. Current state of Fe-Mn-Al-C low density steels. Prog Mater Sci 2017;89:345–91. https://doi.org/10.1016/j.pmatsci.2017.05.002.

[19] Kim C, Terner M, Hong HU, Lee CH, Park SJ, Moon J. Influence of inter/intra-granular κ-carbides on the deformation mechanism in lightweight Fe-20Mn-11.5Al-1.2C steel. Mater Char 2020;161:110142. https://doi.org/10.1016/j.matchar.2020.110142.

[20] Chen P, Li X, Yi H. The κ-carbides in low-density Fe-Mn-Al-C steels: a review on their structure, precipitation and deformation mechanism. Metals 2020;10:1021. https://doi.org/10.3390/met10081021.

[21] Bartlett LN, Aken DC Van, Medvedeva J, Isheim D, Medvedeva N, Song K. An atom probe study of κ-carbide precipitation in austenitic lightweight steel and the effect of phosphorus. Metall Mater Trans A 2017;48:5500–15. https://doi.org/10.1007/s11661-017-4287-3.

[22] Zhi H, Li J, Li W, Elkot M, Antonov S, Zhang H, Lai M. Simultaneously enhancing strength-ductility synergy and strain hardenability via Si-alloying in medium-Al FeMnAlC lightweight steels. Acta Mater 2023;245:118611. https://doi.org/10.1016/j.actamat.2022.118611.

[23] Elkot MN, Sun B, Zhou X, Ponge D, Raabe D. On the formation and growth of grain boundary κ-carbides in austenitic high-Mn lightweight steels. Mater. Res. Lett. 2024;12:10–6. https://doi.org/10.1080/21663831.2023.2284321.

[24] Moon J, Jo HH, Park SJ, Kim SD, Lee TH, Lee CH, Lee MG, Hong HU, Suh DW, Raabe D. Ti-bearing lightweight steel with large high temperature ductility via thermally stable multi-phase microstructure. Mater Sci Eng, A 2021;808:140954. https://doi.org/10.1016/j.msea.2021.140954.

[25] Todaro CJ, Easton MA, Qiu D, Zhang D, Bermingham MJ, Lui EW, Brandt M, StJohn DH, Qian M. Grain structure control during metal 3D printing by high-intensity ultrasound. Nat Commun 2020;11:142. https://doi.org/10.1038/s41467-019-13874-z.

[26] Zheng W, He Y, Yang J, Gao Z. Influence of crystallographic orientation of epitaxial solidification on the initial instability during the solidification of welding pool. J Manuf Process 2019;38:298–307. https://doi.org/10.1016/j.jmapro.2019.01.035.